Thermoelectric and Magnetic Properties of [(Ca$_{1-x}$Pb$_x$)$_2$CoO$_{3.1}$]$_{0.62}$CoO$_2$ (0 $\leqq$ x $\leqq$ 0.03)

Hiroshi NAKATSUGAWA, Hyeon Mook JEONG, Rak Hee KIM[1], and Natsuko GOMI

Graduate School of Engineering, Yokohama National University, 79-5 Tokiwadai, Hodogaya-ku, Yokohama 240-8501, Japan
[1]*School of Advanced Material Engineering, Changwon National University, 9 Sarim-dong, Changwon, Gyeongnam 641-773, Korea*

We have prepared polycrystalline [(Ca$_{1-x}$Pb$_x$)$_2$CoO$_{3.1}$]$_{0.62}$CoO$_2$ (0 $\leqq$ x $\leqq$ 0.03) samples by a conventional solid-state reaction method and investigated the effects of Pb substitution on the thermoelectric and magnetic properties of the samples. With Pb substitution, both electrical resistivity and Seebeck coefficient do not change markedly. This is attributed to the carrier concentration of the samples. Seebeck and Hall coefficient measurements reveal that the major charge carriers in the samples are holes, however, the carrier concentration does not change with increasing x. Neutron powder diffraction and magnetic susceptibility measurements also reveal that Pb ions are in a divalent state in a rock salt-type Ca$_2$CoO$_3$ block layer. The average valence state of Co ions in a CdI$_2$-type CoO$_2$ sheet is 3.1+ and that of Co ions in the block layer is 3.6+. The resulting dimensionless figure of merit for an x = 0.02 sample at room temperature is 0.024, which is approximately equal to the corresponding value of a polycrystalline NaCo$_2$O$_4$ sample. [DOI: 10.1143/JJAP.46.3004]

KEYWORDS: Pb substitution, electrical resistivity, Seebeck coefficient, Hall coefficient, thermoelectric properties, magnetic properties, dimensionless figure of merit

1. Introduction

Since the discovery of a large thermoelectric power in the layered compounds NaCo$_2$O$_4$ and Ca$_3$Co$_4$O$_9$,[1–4] misfit-layered cobalt oxides particularly have attracted considerable interest as candidates for thermoelectric (TE) materials. Figure 1 shows the initial structure model projected in perspective from the b-axis (left) and a-axis (right). As shown in Fig. 1, the crystal structure of Ca$_3$Co$_4$O$_9$ consists of an alternate stack of a distorted three-layered rock salt (RS)-type Ca$_2$CoO$_3$ block layer (BL) and a CdI$_2$-type CoO$_2$ conducting sheet parallel to the c-axis.[3,5,6] The CdI$_2$-type [CoO$_2$] and RS-type [Ca$_2$CoO$_3$] BL subsystems have common a- and c-axes and beta angles, owing to the size difference between the RS-type BL and the CoO$_2$ sheet, the compound has an incommensurate periodicity parallel to the b-axis. The resulting structural formula is [Ca$_2$CoO$_{3+y}$]$_p$-CoO$_2$, where p equals $b_{CoO_2}/b_{Ca_2CoO_3} \sim 0.62$ and $y \sim 0.1$ indicates an oxygen nonstoichiometry. The chemical formula can be approximately represented as Ca$_{1.24}$Co$_{1.62}$O$_{3.86}$. Throughout this paper, we use the structural formula of the compound instead of its chemical formula. Such an anisotropic structure of the compound is believed to be favorable in realizing a large absolute Seebeck coefficient, |S|, and a low thermal conductivity, κ, necessary for appropriate TE compounds. Furthermore, the RS-type BL can be regarded as a charge reservoir, which introduces hole carriers into the CoO$_2$ sheet. In addition, a CoO$_2$ triangular lattice in the CoO$_2$ sheet should play an important role for realizing a low electrical resistivity, ρ, namely, a large TE power factor, $|S|^2/\rho$.

As is well known, the 3d orbital of an octahedrally coordinated Co ion splits into doubly degenerated upper e_g and triply degenerated lower t_{2g} levels. The t_{2g} levels further split into another doubly degenerated e'_g levels and a nondegenerated a_{1g} level owing to the rhombohedral distortion of the octahedron. Since the ^{59}Co NMR studies of metallic NaCo$_2$O$_4$ confirmed that both Co^{3+} and Co^{4+} ions are in the low-spin (LS) states,[7] their electronic configurations are Co^{3+}: $(e'_g)^4(a_{1g})^2$ and Co^{4+}: $(e'_g)^4(a_{1g})^1$, respectively. On the basis of the results of the band calculation of

NaCo$_2$O$_4$,[8] the density of states (DOS) near the Fermi level (E_F) consists of a narrow (localized) a_{1g} band and the broad (itinerant) e'_g band. The height of E_F depends on the nominal valence state of the Co ions. For the case of Co^{3+}, E_F is located at the upper edge of the a_{1g} band, and therefore, a high ρ is expected. With increasing hole carrier concentration, the nominal valence state of the Co ions gradually approaches Co^{4+} and E_F crosses the bands, where a_{1g} and e'_g are hybridized. Thus, a low ρ is then expected for such a mixed valent compound. In addition, a large |S| can also be realized near the compositional region between Co$^{3.1+}$ and Co$^{3.3+}$ because the Seebeck coefficient |S| is roughly expressed using the well-known Mott's formula

$$\frac{|S|}{T} = -\frac{\pi^2 k_B^2}{3e}\left(\frac{\partial \ln \sigma(E)}{\partial E}\right)_{E=E_F}, \qquad (1)$$

where $\sigma(E)$ is proportional to the area of DOS at E_F.

The polycrystalline Ca$_3$Co$_4$O$_9$ sample typically exhibits $|S| \sim 130\,\mu$V/K, $\rho \sim 1.5 \times 10^{-4}\,\Omega$ m, and $\kappa \sim 1.0$ W/mK at room temperature.[4] For practical use, an appreciable decrease in ρ must be achieved because $\rho \sim 1.5 \times 10^{-4}\,\Omega$ m at room temperature is about one order of magnitude higher than that of Bi$_2$Te$_3$-based TE materials. Considerable effort has been devoted to decreasing ρ while maintaining a large |S| and a low κ, through partial substitutions for Ca atoms in the RS-type BL. The optimization of the valence state of Co ions in the RS-type BL is a key issue in maximizing the TE properties because ρ and |S| are highly dependent on the nominal valence state of the Co ions in the CoO$_2$ sheet. In fact, Li et al.[9] and Funahashi et al.[10] reported a marked increase in TE performance due to the partial substitution of Bi for Ca. However, no studies have ever dealt with the effect of the substitution of Pb for Ca. Thus, we have employed a high-resolution neutron powder diffraction technique to investigate the modulated crystal structure of the Pb-doped [Ca$_2$CoO$_{3.1}$]$_{0.62}$CoO$_2$ polycrystalline samples. In this study, we investigate the neutron powder diffraction technique and also the measurements of electrical resistivity, Seebeck coefficient, Hall coefficient, thermal conductivity, and magnetic susceptibility to clarify both the TE properties and the valence state of Co ions.
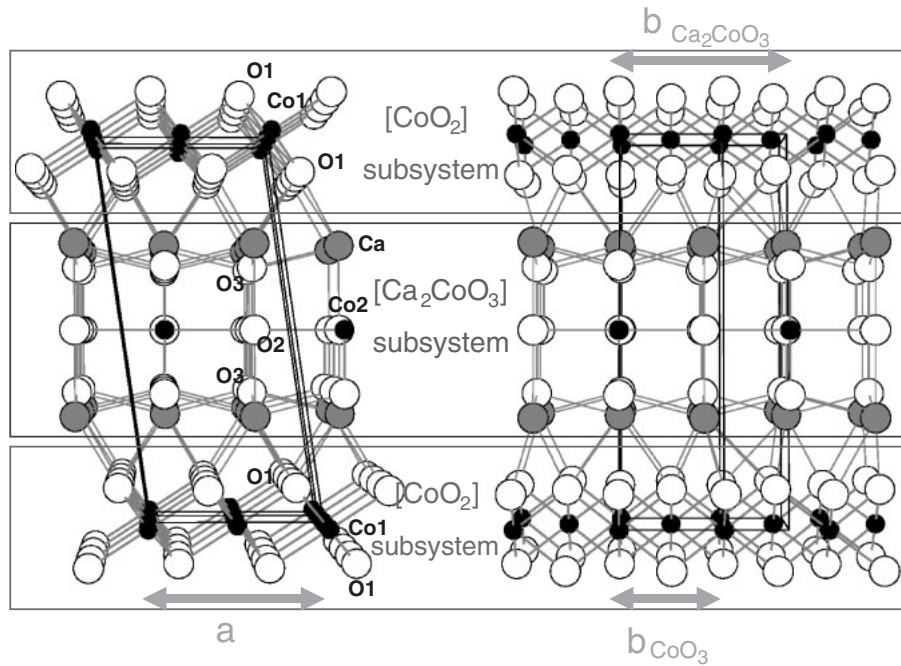
Jpn. J. Appl. Phys., Vol. 46, No. 5A (2007)

H. Nakatsugawa *et al.*

Fig. 1.   Initial structure model of $[Ca_2CoO_{3+y}]_pCoO_2$ projected in perspective from *b*-axis (left) and *a*-axis (right), where *p* equals $b_{CoO_2}/b_{Ca_2CoO_3}$ and $y \sim 0.1$ is oxygen nonstoichiometry.

2.   Experimental Procedure

Polycrystalline $[(Ca_{1-x}Pb_x)_2CoO_{3.1}]_{0.62}CoO_2$ ($0 \leqq x \leqq$ 0.03) samples were prepared by a conventional solid-state reaction method starting from a mixture of $CaCO_3$ (99.9%), PbO (99.9%) and Co_3O_4 (99.9%) powders with a stoichiometric cation ratio. After calcination in air at 920 °C for 12 h, the calcined powders were pressed into pellets and sintered in pure flowing oxygen gas at 920 °C for 24 h. The obtained well-crystallized single-phase samples were annealed in pure flowing oxygen gas at 700 °C for 12 h and then quenched in distilled water to control oxygen nonstoichiometry.[11] By synthesis, the nominal *b*-axis ratio $b_{CoO_2}/b_{Ca_2CoO_3}$ was fixed at about 0.62 in all the samples.

The solubility limit of Pb was determined on the basis of powder X-ray diffraction (XRD) intensities at room temperature using a JEOL JDX-3530 diffractometer (Cu Kα). Neutron powder diffraction (ND) data were collected at room temperature using a Kinken powder diffractometer for the high-efficiency and high-resolution measurements (HERMES) of Institute for Materials Research (IMR), Tohoku University, installed at a JRR-3M reactor in Japan Atomic Energy Research Institute (JAERI), Tokai.[12] Neutrons with a wavelength of 0.18265 nm were obtained by the 331 reflection of a Ge monochromator. The ND data were collected on thoroughly ground powders in a multiscanning mode in the 2θ range from 3.0 to 153.9° with a step width of 0.1° and analyzed using the Rietveld refinement program PREMOS 91,[13] adopting a superspace group of $C2/m(1p0)s0$, where the CdI$_2$-type [CoO$_2$] subsystem has a $C2/m$ symmetry, whereas the RS-type BL [Ca$_2$CoO$_{3.1}$] subsystem has a $C2_1/m$ symmetry. The crystal structures and interatomic distance plots were obtained using the PRJMS and MODPLT routines, respectively; both were implemented in a PREMOS 91 package.

The measurements of electrical resistivity, Seebeck coefficient and Hall coefficient were carried out in the temperature range from 80 to 385 K. The electrical resistivity ρ was measured by a van der Pauw technique with a current of 10 mA in He atmosphere. The Seebeck coefficient $|S|$ measurement was carried out on a sample placed between two blocks of oxygen-free high-conductivity (OFHC) silver. The thermocouples were welded to the reverse sides of the OFHC silver to measure the temperature difference $\Delta T \sim$ 3 K and thermoelectric power ΔV. The slope $(d\Delta V/d\Delta T)$ obtained by a least-squares method yields the Seebeck coefficient $|S|$ at each measurement temperature. The Hall coefficient R_H measurement was performed on flat square pieces of materials with a current of 100 mA in a magnetic field of 8500 Oe by a van der Pauw technique. The Hall carrier concentration *n* was determined from R_H using $n = 1/eR_H$, where *e* is the electron charge, assuming a scattering factor equal to 1 and a single carrier model. Furthermore, the Hall mobility μ was determined from ρ and R_H using $\mu = R_H/\rho$.

Thermal conductivity was measured at room temperature and magnetic susceptibility measurements were carried out in the temperature range from 2 to 350 K. The thermal conductivity κ was calculated from $\kappa = A \cdot C \cdot D$, where *A* is the thermal diffusivity, *C* is the specific heat, and *D* is the measured sample density. The thermal diffusivity was measured by a laser flash method (ULVAC, TC-3000) at room temperature. The magnetic susceptibility χ was measured using a superconducting quantum interference device (SQUID) magnetometer (Quantum Design, MPMS) under zero-field cooling (ZFC) and field cooling (FC) conditions at a magnetic field of 10 Oe.

3.   Results and Discussion

3.1   Thermoelectric properties

Figure 2 shows the temperature dependence of the electrical resistivity $\rho(T)$ of the samples with $[(Ca_{1-x}Pb_x)_2$-
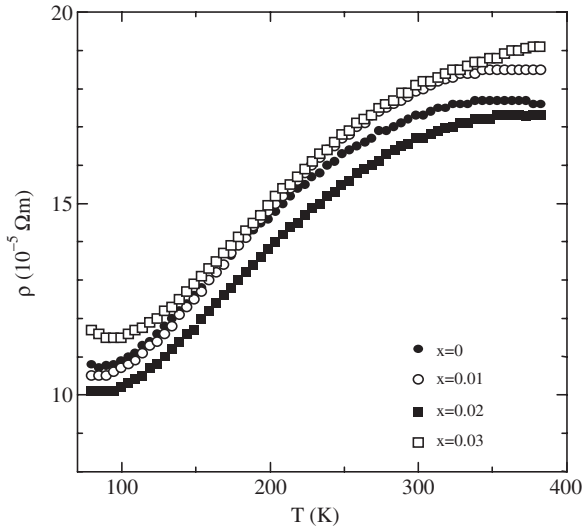
Fig. 2. Temperature dependence of electrical resistivity ρ of $[(Ca_{1-x}$-$Pb_x)_2CoO_{3.1}]_{0.62}CoO_2$ ($0 \leqq x \leqq 0.03$).

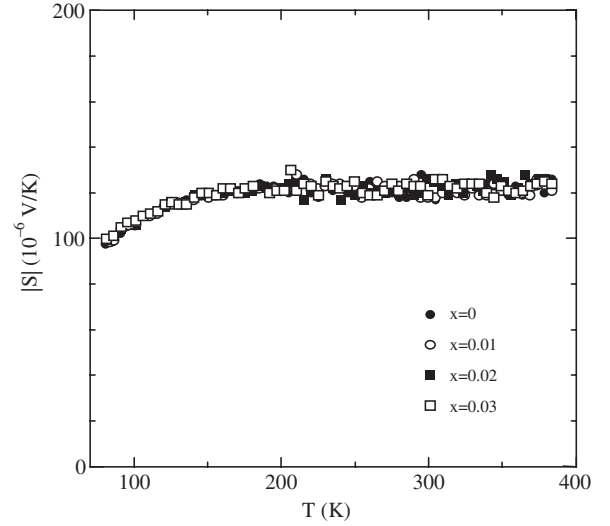Fig. 3. Temperature dependence of Seebeck coefficient $|S|$ of $[(Ca_{1-x}$-$Pb_x)_2CoO_{3.1}]_{0.62}CoO_2$ ($0 \leqq x \leqq 0.03$).

Table I. Electrical resistivity ρ, Hall coefficient R_H, carrier concentration n, Hall mobility μ, Seebeck coefficient $|S|$, power factor $|S|^2/\rho$, thermal diffusivity A, measured sample density D, specific heat C, electronic component of thermal conductivity κ_e, and lattice component of thermal conductivity κ_L at room temperature.

	$x = 0$	$x = 0.01$	$x = 0.02$	$x = 0.03$
ρ (10^{-5} Ω m)	17.3	17.9	16.7	18.1
R_H (10^{-9} m^3 C^{-1})	11.2	11.1	11.3	11.0
n (10^{26} m^{-3})	5.58	5.65	5.52	5.70
μ (10^{-5} m^2 V^{-1} s^{-1})	6.4	6.0	6.6	5.9
$|S|$ (10^{-6} V K^{-1})	119	118	126	119
$|S|^2/\rho$ (10^{-4} W m^{-1} K^{-2})	0.82	0.78	0.95	0.78
A (10^{-7} m^2 s^{-1})	6.28	5.93	6.04	6.31
D (10^3 kg m^{-3})	3.20	3.18	3.25	3.33
C (10^2 J kg^{-1} K^{-1})	6.16	6.27	6.18	6.13
κ_e (W m^{-1} K^{-1})	0.04	0.04	0.04	0.04
κ_L (W m^{-1} K^{-1})	1.20	1.14	1.17	1.25
ZT	0.020	0.020	0.024	0.018

CoO$_{3.1}$]$_{0.62}$CoO$_2$ ($0 \leqq x \leqq 0.03$) measured in the temperature range from 80 to 385 K. In particular, the sample with $x = 0.02$ shows the lowest electric resistivity (1.67×10^{-4} Ωm) at room temperature. All the samples show a metallic behavior down to around 90–100 K. With a further decrease in temperature, the samples exhibit a semiconducting behavior owing to the carrier localization of a ferrimagnetic transition at around 20 K and the possible occurrence of a spin density wave (SDW) at around 100 K.[14] Sugiyama *et al.*[14] have suggested that the Co^{4+}: $(e'_g)^4(a_{1g})^1$ ions in the RS-type BL include an SDW transition. Furthermore, it is reported that a ferrimagnetic transition originates from the modulated magnetic sublattices of Co^{4+} ions in the BL subsystem.[14] Table I shows a summary of the electrical resistivities obtained at room temperature.

The temperature dependence of the absolute Seebeck coefficient $|S(T)|$ is shown in Fig. 3. It can be observed clearly that at temperatures above 100 K, the Seebeck coefficient of the $[(Ca_{1-x}Pb_x)_2CoO_{3.1}]_{0.62}CoO_2$ samples

shows a weak temperature dependence. We have confirmed that all the samples are found to show a similar $|S|$. The effect of Pb^{2+} substitution on $|S|$ could be interpreted using the framework of the model proposed to explain the large Seebeck coefficient of the NaCo$_2$O$_4$. In this model, the Seebeck coefficient of high-temperature limit can be estimated using the modified Heikes formula[15]

$$S(T \rightarrow \infty) = -\frac{k_B}{e} \ln\left[\frac{g_3}{g_4} \frac{c}{1-c}\right], \qquad (2)$$

where g_3 and g_4 are the numbers of the degenerated configurations of the Co^{3+} and Co^{4+} states in the CoO$_2$ sheet, respectively, whereas $c = $ Co^{4+}/Co is the fraction of Co^{4+} holes at the Co sites in the [CoO$_2$] subsystem. Since the electronic configurations of the Co^{3+} and Co^{4+} ions are in the low spin state, the numbers of the degenerated configurations of the Co^{3+} and Co^{4+} states in the CoO$_2$ sheet are $g_3 = 1$ and $g_4 = 6$, respectively. Thus, on the basis of the above-mentioned formula, the $S(T \rightarrow \infty)$ values remain constant with no change in c. In this study, the substitution of divalent Pb^{2+} for divalent Ca^{2+} maintains the hole concentrations $c \sim 0.1$. Therefore, the $[(Ca_{1-x}Pb_x)_2$-CoO$_{3.1}]_{0.62}CoO_2$ samples show similar $|S|$ values, as shown in Fig. 3.

The TE power factor $|S|^2/\rho$ of $[(Ca_{1-x}Pb_x)_2CoO_{3.1}]_{0.62}$-CoO$_2$ ($0 \leqq x \leqq 0.03$) as a function of temperature is represented in Fig. 4. The $|S|^2/\rho$ values at room temperature are summarized in Table I. In particular, the sample with $x = 0.02$ exhibits the largest TE power factor of 9.5×10^{-5} W/mK^2 at room temperature and a broad maximum at around 100–150 K. With a further decrease in temperature, the $|S|^2/\rho$ value decreases gradually. Since the Seebeck coefficient $|S(T)|$ behavior does not change markedly, as we previously mentioned, the TE power factor primarily depends on the electrical resistivity $\rho(T)$.

Figure 5 shows the temperature dependence of the Hall coefficient $R_H(T)$ of the samples with $[(Ca_{1-x}Pb_x)_2$-CoO$_{3.1}]_{0.62}CoO_2$ ($0 \leqq x \leqq 0.03$) measured in the temperature range from 80 to 385 K. All the samples show $R_H = +11 \times 10^{-9}$ m^3/C at room temperature. Hall coefficient
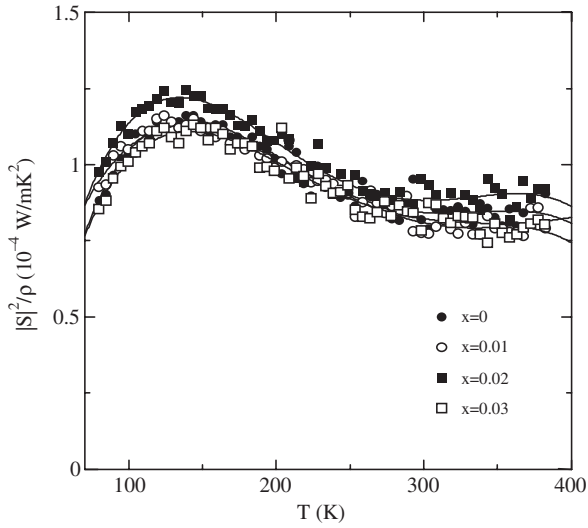
Fig. 4. Temperature dependence of power factor $|S|^2/\rho$ of $[(Ca_{1-x}Pb_x)_2\text{-}CoO_{3.1}]_{0.62}CoO_2$ $(0 \leqq x \leqq 0.03)$.

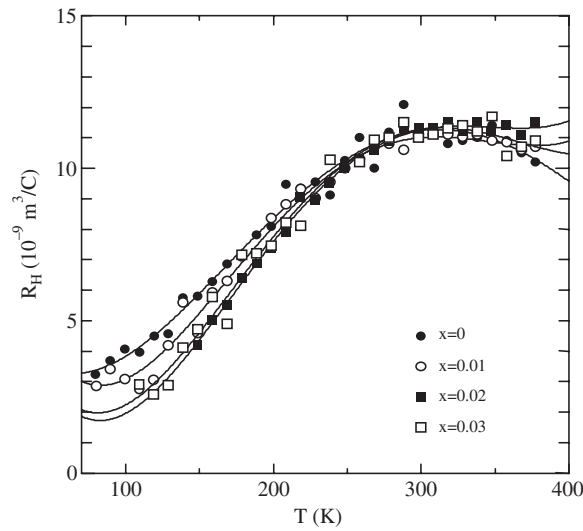
Fig. 5. Temperature dependence of Hall coefficient R_H of $[(Ca_{1-x}Pb_x)_2\text{-}CoO_{3.1}]_{0.62}CoO_2$ $(0 \leqq x \leqq 0.03)$.

measurements reveal that the major charge carriers in all the samples are holes. Moreover, the signs of Hall coefficient are consistent with those of Seebeck coefficient. The Hall coefficient R_H, Hall carrier concentration $n = 1/eR_H$, and Hall mobility $\mu = R_H/\rho$ at room temperature are also summarized in Table I, where the Hall carrier concentration of $[(Ca_{1-x}Pb_x)_2CoO_{3.1}]_{0.62}CoO_2$ $(0 \leqq x \leqq 0.03)$ is about 6×10^{26} m^{-6} at room temperature.

The thermal conductivity κ can be expressed by the sum of the lattice component κ_L and electronic component κ_e, which is estimated from Wiedemann–Franz's law as $\kappa_e = LT/\rho$, where L is the Lorentz number ($L \sim 2.44 \times 10^{-8}$ V^2/K^2 for free electrons). The thermal diffusivity, measured density, specific heat, electronic thermal conductivity, lattice thermal conductivity, and dimensionless TE figure of merit $ZT = |S|^2T/\rho\kappa$ for all the samples at room temperature are summarized in Table I. κ_e remains constant at 0.04 W/mK for all the samples, whereas κ_L is minimum ($\kappa_L = 1.14$ W/mK) at $x = 0.01$. In addition, κ_L at room temperature is approximately 30% smaller than that reported for (Na, Ca)-

Table II. Initial structure model for $x = 0$.

[CoO2] sheet	$x\ (= x_1)$	$y\ (= x_2)$	$z\ (= x_3)$	B (Å^2)
Co1	0	0	0	1.0
O1	0.3612	0	0.0968	1.0
RS-type BL subsystem	$x\ (= x_1)$	$y\ (= x_4)$	$z\ (= x_3)$	B (Å^2)
Ca	0.3167	0	0.7187	1.0
Co2	3/4	0	1/2	1.0
O2	1/4	0	1/2	1.0
O3	0.6977	0	0.3379	1.0

Table III. Refined Fourier amplitudes of fractional coordinates and thermal parameters, B, for $x = 0$.

[CoO2]sheet		A_0	A_1	B_1	A_2	B_2
Co1	x	0	−0.028(7)	0	0	0
	y	0	0	0	0	0
	z	0	0	0	0	0
	B	−0.9(9)				
O1	x	0	−0.018(1)	0	−0.004(3)	0
	y	0	0	0.046(9)	0	0.005(8)
	z	0	−0.010(2)	0	0	0
	B	−1.5(9)				
RS-type BL subsystem		A_0	A_1	B_1	A_2	B_2
Ca	x	0	−0.019(2)	0	0.023(3)	0
	y	0	0	−0.008(4)	0	0
	z	0	−0.004(6)	0	−0.006(9)	0
	B	−0.7(0)				
Co2	x	0	0.136(5)	0	0	0
	y	0	0	0	0	0.001(4)
	z	0	−0.005(1)	0	0	0
	B	−0.6(1)				
O2	x	0	0.078(7)	0	0	0
	y	0	0	0	0	0.093(0)
	z	0	0	0	0	0
	B	0.6(7)				
O3	x	0	−0.016(3)	0	−0.015(3)	0
	y	0	0	0.005(4)	0	0
	z	0	−0.016(2)	0	0.008(6)	0
	B	−1.6(3)				

Co$_2$O$_4$[16] because $[(Ca_{1-x}Pb_x)_2CoO_{3.1}]_{0.62}CoO_2$ $(0 \leqq x \leqq 0.03)$ has a misfit structure; the $[CoO_2]$ and $[(Ca_{1-x}Pb_x)_2\text{-}CoO_{3.1}]$ subsystems are incommensurate to each other, and thus, very few phonon waves can propagate along the c-axis. This indicates that the phonon mean free path is much shorter than the electron mean free path; $[(Ca_{1-x}\text{-}Pb_x)_2CoO_{3.1}]_{0.62}CoO_2$ $(0 \leqq x \leqq 0.03)$ acts as a material of "the phonon glass and electron crystal" named by Slack.[17] Moreover, the minimum value at $x = 0.01$ indicates that the effect of Pb substitution is related to the modulated crystal structure of $[(Ca_{1-x}Pb_x)_2CoO_{3.1}]_{0.62}CoO_2$ $(0 \leqq x \leqq 0.03)$.

3.2 Crystal structure refinement

Table II shows a summary of the corresponding fractional coordinates of the atoms in $[Ca_2CoO_{3.1}]_{0.62}CoO_2$ $(x = 0)$. In the refinement procedure, the thermal displacement parameter B of each atom was assumed to be isotropic. After two
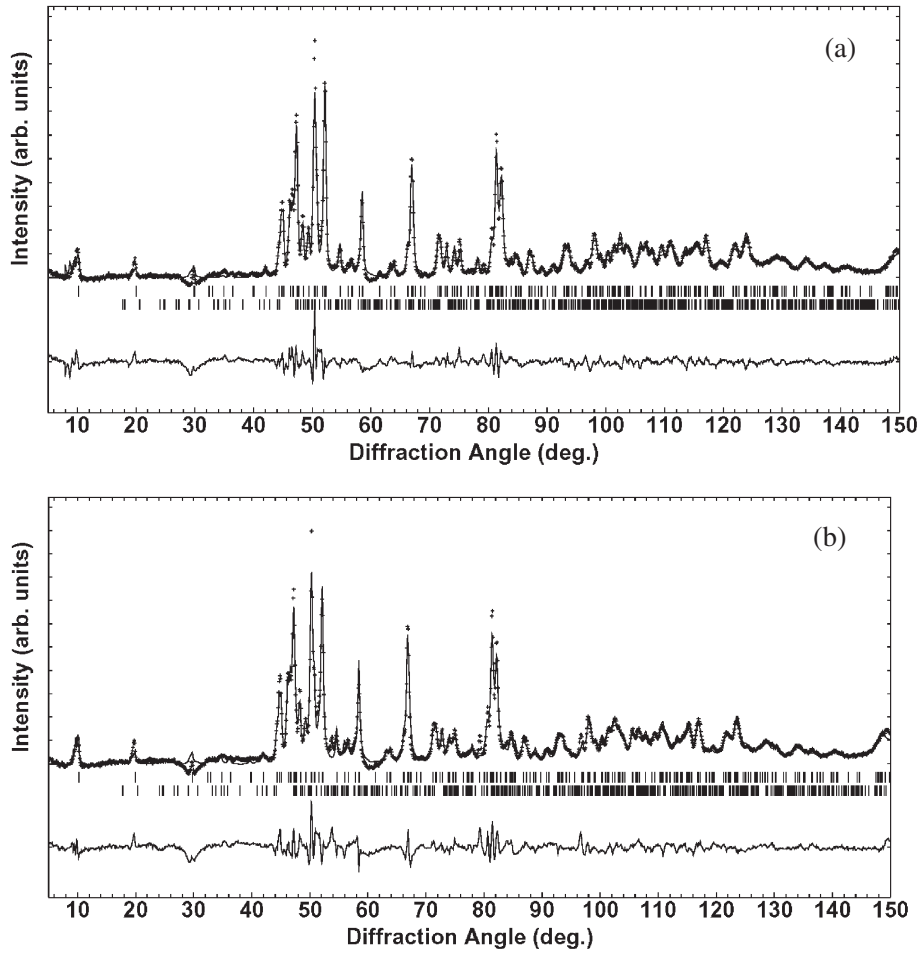
Fig. 6.   Observed, calculated and difference intensities of powder neutron diffraction data (HERMES data) for (a) $x = 0$ (top) and (b) $x = 0.02$ (bottom). Short vertical lines below the intensities indicate the peak positions of the main (upper) and satellite (lower) reflections for the CdI$_2$-type [CoO$_2$] and RS-type [Ca$_2$CoO$_3$] BL subsystems. The differences between the observed and calculated patterns are shown below the vertical lines.

or three refinement cycles, the modulation of the atomic positions in [Ca$_2$CoO$_{3.1}$]$_{0.62}$CoO$_2$ was introduced, considering up to the second order of cosine and sine components of the Fourier terms, i.e., A_i $(i = 0, 1, 2)$ and B_i $(i = 1, 2)$. Table III shows a summary of the refined Fourier amplitudes of the positional parameters. Figure 6(a) shows the observed, calculated and difference intensities of the HERMES data for $x = 0$. Short vertical lines below the patterns indicate the peak positions of the main (upper) and satellite (lower) reflections of the two subsystems. The final R_{wp} factor is 7.3% and the lattice parameters are refined to $a = 0.48404(4)$ nm, $b_{CoO_2} = 0.28262(3)$ nm, $c = 1.08641(4)$ nm and $\beta = 98.18(8)°$ for the [CoO$_2$] subsystem and $b_{RS} = 0.45709(2)$ nm for the RS-type BL subsystem. The resulting $p = b_{CoO_2}/b_{Ca_2CoO_3} = 0.6183(0)$ corresponds to the structural formula [Ca$_2$CoO$_{3.1}$]$_{0.6183}$CoO$_2$.

The crystal structure of [(Ca$_{0.98}$Pb$_{0.02}$)$_2$CoO$_{3.1}$]$_{0.62}$CoO$_2$ $(x = 0.02)$ was also analyzed in a similar manner using the identical structure model as shown in Table IV. We assumed that the Pb atoms can only substitute for Ca. sites. Figure 6(b) shows the observed, calculated and difference intensities of the HERMES data for $x = 0.02$. Table V shows a summary of the refined Fourier amplitudes of the positional parameters. The final R_{wp} factor is 8.0% and the lattice parameters are refined to $a = 0.48384(3)$ nm, $b_{CoO_2} =$

Table IV.   Initial structure model for $x = 0.02$.

[CoO$_2$] sheet	x ($= x_1$)	y ($= x_2$)	z ($= x_3$)	B (Å^2)
Co1	0	0	0	1.0
O1	0.3626	0	0.0986	1.0
RS-type BL subsystem	x ($= x_1$)	y ($= x_4$)	z ($= x_3$)	B (Å^2)
Ca	0.3254	0	0.7251	1.0
Co2	3/4	0	1/2	1.0
O2	1/4	0	1/2	1.0
O3	0.6967	0	0.3361	1.0

$0.28248(1)$ nm, $c = 1.08865(6)$ nm, and $\beta = 98.19(1)°$ for the [CoO$_2$] subsystem and $b_{RS} = 0.45786(7)$ nm for the RS-type BL subsystem. The resulting $p = b_{CoO_2}/b_{Ca_2CoO_3} = 0.6169(5)$ corresponds to the stoichiometry of the $x = 0.02$ sample, i.e., [(Ca$_{0.98}$Pb$_{0.02}$)$_2$CoO$_{3.1}$]$_{0.6169}$CoO$_2$.

The variation in atomic positional modulation amplitude can be further understood by the plot against t', a complementary coordinate in the (3+1)-dimensional superspace.[13] In the present samples, t' is defined as $-px_2 + x_4 \simeq -0.62x_2 + x_4$. Figure 7 shows Co1–O (upper panels) distances in the [CoO$_2$] subsystem and Co2–O (lower panels) distances in the RS-type subsystem of (a) $x = 0$

Jpn. J. Appl. Phys., Vol. 46, No. 5A (2007)

H. NAKATSUGAWA *et al.*

Table V. Refined Fourier amplitudes of fractional coordinates and thermal parameters, B, for $x = 0.02$.

[CoO2]sheet		A_0	A_1	B_1	A_2	B_2
Co1	x	0	0.020(8)	0	0	0
	y	0	0	0	0	0
	z	0	0	0	0	0
	B	0.1(4)				
O1	x	0	−0.010(0)	0	0.002(9)	0
	y	0	0	0.047(8)	0	0.013(4)
	z	0	−0.003(3)	0	0	0
	B	−0.4(5)				
RS-type BL subsystem		A_0	A_1	B_1	A_2	B_2
Ca	x	0	−0.023(5)	0	0.044(4)	0
	y	0	0	0.020(8)	0	−0.004(9)
	z	0	0.025(8)	0	0.007(8)	0
	B	−1.0(1)				
Co2	x	0	−0.022(8)	0	0	0
	y	0	0	0	0	0.065(4)
	z	0	−0.017(2)	0	0	0
	B	−1.7(1)				
O2	x	0	−0.126(8)	0	0	0
	y	0	0	0	0	0.090(5)
	z	0	0	0	0	0
	B	−0.2(1)				
O3	x	0	−0.025(5)	0	−0.019(1)	0
	y	0	0	−0.015(2)	0	0.002(2)
	z	0	−0.021(0)	0	0.009(4)	0
	B	−1.5(6)				

(left) and (b) $x = 0.02$ (right) plotted against t'. The Co2 site at $z = 1/2$ has six oxygen neighbors, with four equatorial O2 atoms and two apical O3 atoms. Among these bonds, two apical Co2–O3 bonds are relatively shorter than the other four equatorial Co2–O2 bonds, ranging from 0.17 to 0.195 nm for $x = 0$ and from 0.165 to 0.19 nm for $x = 0.02$. The mean distance of the Co2–O3 bonds for $x = 0$ does not change markedly as that of the Co2–O3 bonds for $x = 0.02$, i.e., both distances are 0.18 nm. This finding indicates that the Co ions in the RS-type subsystem are not replaced by tetravalent lead ions in the x range from 0 to 0.02. On the other hand, the four equatorial Co2–O2 bonds for $x = 0$ (lower left panel) show small modulation amplitudes from 0.205 to 0.275 nm, relative to those for $x = 0.02$ (lower right panel) with modulation amplitudes from 0.18 to 0.3 nm. However, the mean distances of the Co2–O2 bonds of the two phases are identical, i.e., 0.24 nm. In contrast to the Co2–O bonds, the six Co1–O1 bonds illustrated in the upper panels remain stable with increasing x, where the mean distance of the Co1–O1 bonds is 0.19 nm.

Relative to the Co–O distances, the (Ca,Pb)–O distances exhibit a marked change, owing to the Pb substitution, as demonstrated in Figs. 8(a) and 8(b). As illustrated in Fig. 8, the (Ca,Pb) sites at $z = 0.72-0.73$ are coordinated to an apical O2 atom and four equatorial O3 atoms in the RS-type subsystem (see lower panels) and three O1 atoms in the [CoO2] subsystem (see upper panels). The (Ca,Pb)–O1 distances vary, as shown in the upper panels. In contrast, the (Ca,Pb)–O2 and (Ca,Pb)–O3 distances vary, as illustrated in

the lower panels. Since the O2 and O3 atoms belong to the same RS-type subsystem, the Ca–O2 and Ca–O3 distances in $x = 0$ are moderately altered between 0.23 and 0.26 nm (lower left panel) with a mean distance of 0.245 nm, which is comparable to the typical ionic Ca–O bond length.[18] The (Ca,Pb)–O2 and (Ca,Pb)–O3 distances for $x = 0.02$ shift to a considerably larger range from 0.215 to 0.283 nm (lower right panel), thus, the mean distance of the five bonds changes markedly (2.49 nm). This finding indicates that the divalent Ca^{2+} ions are partially replaced by the divalent Pb^{2+} ions with increasing x.

Lead ions are in either the divalent state or the tetravalent state in the RS-type BL subsystem. In the case of Pb^{2+}, the ionic radius is 0.129 nm[19] (coordination number, CN = 8). As the ionic radius of Ca^{2+} (0.112 nm, CN = 8) is nearly equal to that of Pb^{2+}, it is reasonable to consider that Ca^{2+} is partially replaced by Pb^{2+}. On the other hand, lead ions must be Pb^{4+} in the Co2 site because some of the Co2–O bond lengths, i.e., the mean distance of the Co2–O3 bonds is as small as 0.18 nm. To account for such a small bond length (0.18 nm), the majority of Pb ions should be in the tetravalent state with an ionic radius of 0.0775 nm (CN = 6), although this ionic radius is much larger than that of low-spin Co^{3+} (0.0545 nm, CN = 6). It is not possible to substitute Pb^{4+} at the Co2 site in $x = 0.02$ because the Co2–O3 modulation amplitude for $x = 0.02$ hardly changes relative to that for $x = 0$, as shown in the lower panels in Fig. 7. Thus, Pb ions are in the least divalent state, i.e., Pb^{2+} in the x range from 0 to 0.02. However, the Co2–O3 modulation amplitude for $x = 0.03$ markedly changes relative to that for $x = 0$. This indicates that the Pb^{4+} ions partially substitute the Co ions in the RS-type BL subsystem of $x = 0.03$ as little as possible.

3.3 Magnetic susceptibilities

Let us evaluate the valence state of Co ions in $[(Ca_{1-x}-Pb_x)_2CoO_{3.1}]_{0.62}CoO_2$ ($0 \leqq x \leqq 0.03$), assuming that the valence state of the substituted lead ions is mainly divalent Pb^{2+}. Sugiyama *et al.*[14] have suggested that a polycrystalline $Ca_3Co_4O_9$ sample exhibits ferrimagnetic transition at $T_C \simeq 19$ K, owing to the antiferromagnetic (AF) order of Co1 in the [CoO2] subsystem and Co2 in the RS-type BL subsystem. Figure 9 shows the temperature dependence of the inverse-magnetic susceptibility $(\chi - \chi_0)^{-1}$ for (a) $x = 0$ and (b) $x = 0.02$ measured under the ZFC condition at a magnetic field of 10 Oe. As shown in Fig. 9, both samples exhibit a positive curvature characteristic of the ferrimagnetic compound. On the basis of mean-field-approximation theory,[20] the magnetic susceptibility can be expressed as

$$\chi = \chi_0 + \frac{(C_{Co1} + C_{Co2})T - 2T_C\sqrt{C_{Co1} \cdot C_{Co2}}}{T^2 - T_C^2}, \quad (3)$$

where χ_0 is the temperature-independent term and C_{Co1} and C_{Co2} are the Curie constants of Co ions contributed by the [CoO2] and [Ca2CoO3.1] subsystems, respectively. The effective magnetic moment of each Co site is then determined using the obtained Curie constant in the equation

$$\mu_{eff} = \sqrt{\frac{3k_B C_{Co1}}{N_A \mu_B}} \quad \text{or} \quad \sqrt{\frac{3k_B C_{Co2}}{N_A \mu_B}}, \quad (4)$$
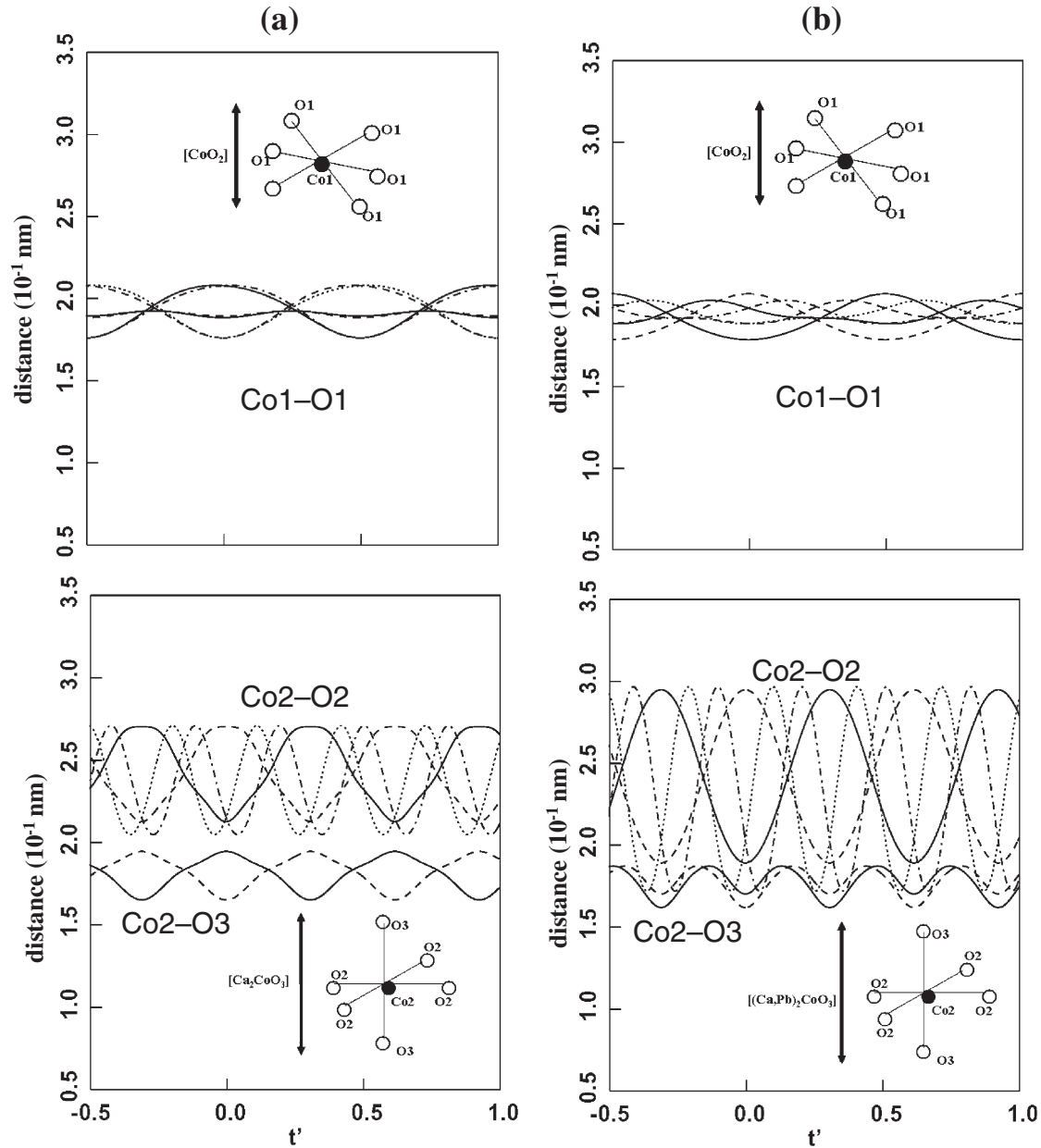
(a)

(b)

Fig. 7.   Six Co1–O1 distances (top left and right), four Co2–O2 distances (bottom left and right) and two Co2–O3 distances (bottom left and right) against complementary coordinate $t' = -px_2 + x_4 \simeq -0.62x_2 + x_4$ in superspace for (a) $x = 0$ (left) and (b) $x = 0.02$ (right).

Table VI.   Curie constants (C_{Co1} and C_{Co2}), spin quantum numbers (S_{Co1} and S_{Co2}), average valence states of Co ions (n_{Co1} and n_{Co2}), and resulting nominal valence state of Co ions for $[(Ca_{1-x}Pb_x)_2CoO_{3.1}]_{0.62}CoO_2$ ($0 \leqq x \leqq 0.03$).

	$x = 0$	$x = 0.01$	$x = 0.02$	$x = 0.03$
C_{Co1} [emu K/mol(Co)$^{-1}$]	0.028	0.034	0.037	0.020
C_{Co2} [emu K/mol(Co)$^{-1}$]	0.220	0.200	0.215	0.200
S_{Co1}	0.053	0.064	0.069	0.039
S_{Co2}	0.332	0.306	0.325	0.306
n_{Co1}	3.11	3.13	3.14	3.08
n_{Co2}	3.66	3.61	3.65	3.61
Average valence state	3.32	3.31	3.33	3.28

where k_B, μ_B, and N_A are the Boltzmann constant, the Bohr magnetron, and Avogadro's number, respectively. From the ^{59}Co NMR studies of NaCo$_2$O$_4$,[7] both Co1 and Co2 sites

consist of a mixture of low-spin Co^{3+} ($S = 0$) and Co^{4+} ($S = 1/2$). Hence, the average valence state of each Co ion (n_m) can be directly derived from $S_m = n_m/2$ using the formula $\mu_{eff} = g\sqrt{S_m(S_m + 1)}$, where we assume $g = 2.0$.

By appropriately fitting the $(\chi - \chi_0)^{-1}$ data above 30 K, for example, we obtained $C_{Co1} = 0.037$ and $C_{Co2} = 0.215$ emu·K/mol(Co) for $x = 0.02$. Using these parameters, the average valence state of Co ions was determined to be $n_{Co1} = 3.14$ and $n_{Co2} = 3.65$ for $x = 0.02$. The resulting nominal valence state of Co ions, i.e., $(n_{Co1} + n_{Co2} \times 0.62)/1.62 \simeq 3.33$, shows a good agreement with the calculated value of 3.30, on the basis of the charge neutrality of the chemical formula Ca$_{1.22}$Pb$_{0.025}$Co$_{1.62}$O$_{3.92}$. The Curie constants (C_{Co1} and C_{Co2}), the spin quantum numbers (S_{Co1} and S_{Co2}), the average valence states of Co ions (n_{Co1} and n_{Co2}) and the resulting nominal valence state of Co ions for $[(Ca_{1-x}Pb_x)_2CoO_{3.1}]_{0.62}CoO_2$ ($0 \leqq x \leqq 0.03$) are summariz-
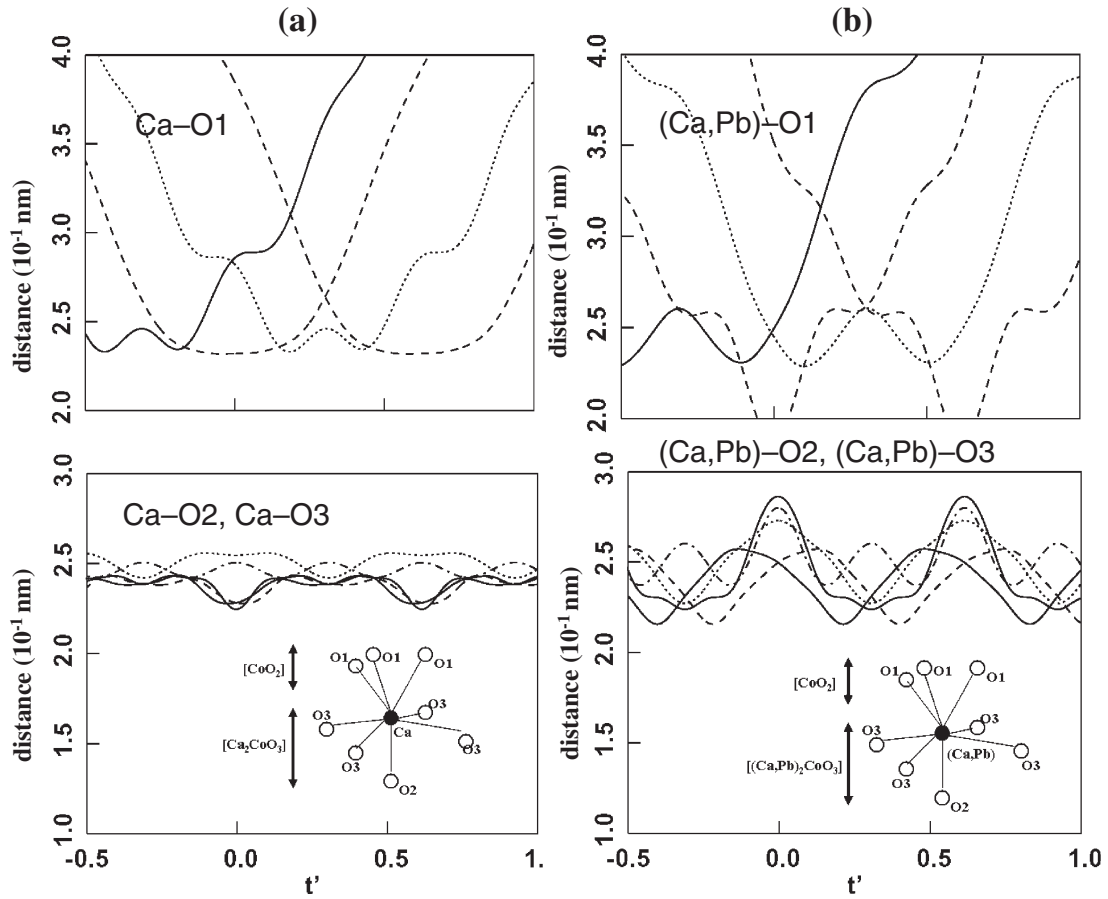
Fig. 8. Three Ca–O1 distances (top left), Ca–O2 distance (bottom left) and four Ca–O3 distances (bottom left) against complementary coordinate $t' = -px_2 + x_4 \simeq -0.62x_2 + x_4$ in superspace for (a) $x = 0$ (left). Three (Ca,Pb)–O1 distances (top right), (Ca,Pb)–O2 distance (bottom right) and four (Ca,Pb)–O3 distances (bottom right) against complementary coordinate t' in superspace for (b) $x = 0.02$ (right).
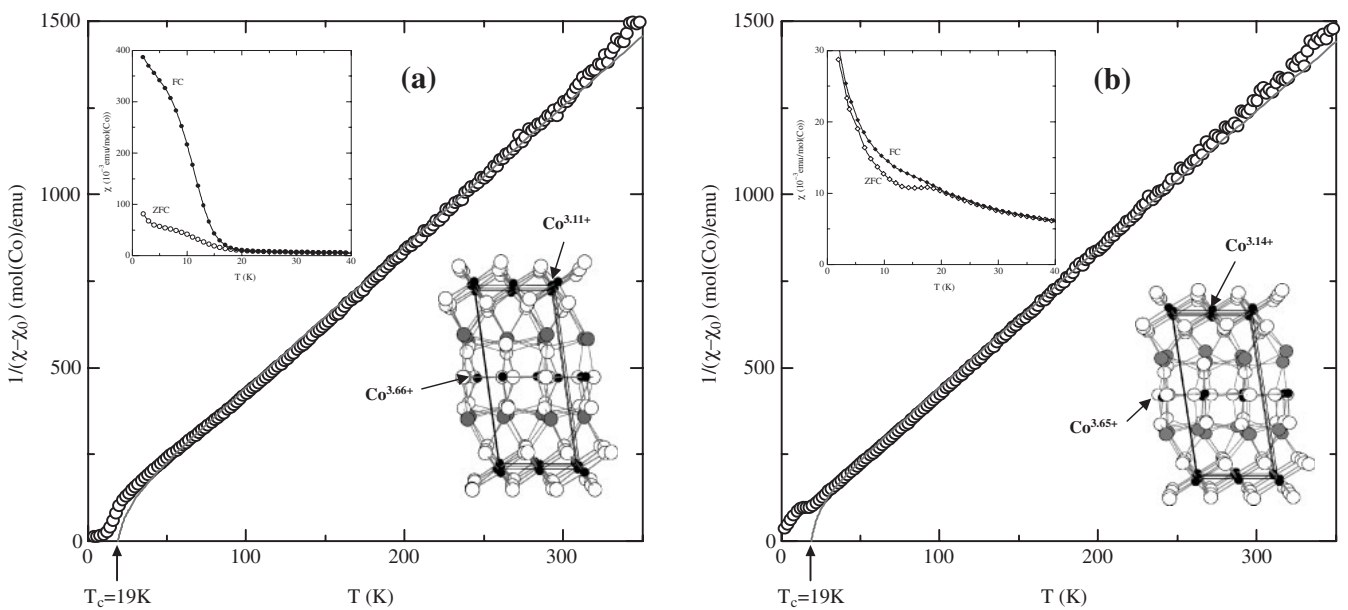

Fig. 9. Temperature dependence of inverse magnetic susceptibility $(\chi - \chi_0)^{-1}$ for (a) $x = 0$ (left) and (b) $x = 0.02$ (right), where red line shows result of appropriately fitting $(\chi - \chi_0)^{-1}$ data, where $\chi_0 \sim 7 \times 10^{-4}$ emu/mol(Co) is temperature-independent term and $T_C = 19$ K is ferrimagnetic transition temperature. The inset shows the temperature dependence of the magnetic susceptibility χ in a magnetic field of 10 Oe under the ZFC (open circles) and FC (solid circles) conditions for (a) $x = 0$ (left) and (b) $x = 0.02$ (right).

Jpn. J. Appl. Phys., Vol. 46, No. 5A (2007)

H. NAKATSUGAWA *et al.*

ed in Table VI. Therefore, a low ρ is then expected for the mixed valent of the Co1 site, i.e., $Co^{3+}_{0.9}Co^{4+}_{0.1}$. In addition, a large $|S|$ can also be realized because the DOS near E_F consists of the a_{1g} and e'_g bands in the electronic state of $Co^{3.1+}$. As evidenced, the hole concentration at the Co1 site remains constant with increasing x, which is consistent with the results for $|S(T)|$ and $R_H(T)$.

4. Conclusions

Polycrystalline $[(Ca_{1-x}Pb_x)_2CoO_{3.1}]_{0.62}CoO_2$ ($0 \leqq x \leqq 0.03$) samples have been prepared using a conventional solid-state reaction method, and the effect of Pb substitution on the TE properties of the samples have been studied. The sample with $x = 0.02$ shows a rather low ρ and a large $|S|$, suggesting that it is a promising TE material. Thermal conductivity at room temperature shows a small κ in all the samples. Thus, the maximum ZT is 0.024 in $x = 0.02$ at room temperature. Seebeck coefficient shows a similar large $|S|$ in all the samples because the substitution of Pb^{2+} for Ca^{2+} maintains the carrier (holes) concentration. In fact, the Co2–O3 modulation amplitude reveals that Pb ions are mainly Pb^{2+} in the RS-type BL subsystem. Magnetic susceptibility measurements also show that the Co1 and Co2 sites are in the average valence states of $Co^{3.1+}$ and $Co^{3.6+}$, respectively. This suggests that Pb ions can hardly be Pb^{4+} in the RS-type BL subsystem of all the samples.

Acknowledgments

1) I. Terasaki, Y. Sasago, and K. Uchinokura: Phys. Rev. B **56** (1997) R12685.
2) S. Li, R. Funahashi, I. Matsubara, K. Ueda, and H. Yamada: J. Mater. Chem. **9** (1999) 1659.
3) A. C. Masset, C. Michel, A. Maignan, M. Hervieu, O. Toulemomde, F. Aruder, B. Raveau, and J. Hejtmanek: Phys. Rev. B **62** (2000) 166.
4) Y. Miyazaki, K. Kudo, M. Akoshima, Y. Ono, Y. Koike, and T. Kajitani: Jpn. J. Appl. Phys. **39** (2000) L531.
5) S. Lambert, H. Leligny, and D. Grebille: J. Solid State Chem. **160** (2001) 322.
6) Y. Miyazaki, M. Onoda, T. Oku, M. Kikuchi, Y. Ishii, Y. Ono, Y. Morii, and T. Kajitani: J. Phys. Soc. Jpn. **71** (2002) 491.
7) R. Ray, A. Ghoshray, K. Ghoshray, and S. Nakamura: Phys. Rev. B **59** (1999) 9454.
8) D. J. Singh: Phys. Rev. B **61** (2000) 13397.
9) S. Li, R. Funahashi, I. Matsubara, K. Ueno, S. Sodeoka, and H. Yamada: Chem. Mater. **12** (2000) 2424.
10) R. Funahashi, I. Matsubara, H. Ikuta, T. Takeuchi, U. Mizutani, and S. Sodeoka: Jpn. J. Appl. Phys. **39** (2000) L1127.
11) J. Shimoyama, S. Horii, K. Otzschi, M. Sano, and K. Kishio: Jpn. J. Appl. Phys. **42** (2003) L194.
12) K. Ohoyama, T. Kanouchi, K. Nemoto, M. Ohashi, T. Kajitani, and Y. Yamaguchi: Jpn. J. Appl. Phys. **37** (1998) 3319.
13) A. Yamamoto: Acta Crystallogr., Sect. A **49** (1993) 831.
14) J. Sugiyama, H. Itahara, T. Tani, J. H. Brewer, and E. J. Ansaldo: Phys. Rev. B **66** (2002) 134413.
15) W. Koshibae, K. Tsutsui, and S. Maekawa: Phys. Rev. B **62** (2000) 6869.
16) K. Takahata, Y. Iguchi, T. Itoh, D. Tanaka, and I. Terasaki: Phys. Rev. B **61** (2000) 12551.
17) G. A. Slack: in *CRC Handbook of Thermoelectrics*, ed. D. M. Rowe (CRC Press, Boca Raton, 1995) p. 407.
18) R. W. G. Wyckoff: *Crystal Structures* (Wiley-Interscience, New York, 1963) Vol. 1, p. 86.
19) R. D. Shannon: Acta Crystallogr., Sect. A **32** (1976) 751.
20) C. Kittel: *Introduction to Solid State Physics* (John Wiley & Sons, New York, 1996) 7th ed. p. 461.